Corrosion Science 157 (2019) 51–61

Contents lists available at ScienceDirect

Corrosion Science

journal homepage: www.elsevier.com/locate/corsci

Kinetics of corrosion-driven cathodic disbondment on organic coated trivalent chromium metal-oxide-carbide coatings on steel

James E. Edy[a], Hamilton N. McMurray[a], Koen R. Lammers[b], Arnoud C.A. deVooys[b]

[a] Swansea University, Materials Research Centre, College of Engineering, Bay Campus, Swansea, SA1 8EN, United Kingdom
[b] Tata Steel, Research & Development, IJmuiden Technology Centre, P.O. Box 10.000, 1970CA, IJmuiden, The Netherlands

ARTICLE INFO

Keywords:
Steel
Chromium
Cathodic disbondment
Oxygen reduction
Chrome-free

ABSTRACT

Chromium metal-oxide-carbide coatings of varying composition and thickness, cathodically electrodeposited from a Cr (III)-formate electrolyte are compared for their ability to resist the corrosion driven delamination of an adherent polymer overcoat. Cathodic disbondment rates are determined using an in-situ scanning Kelvin probe technique. The rates of cathodic disbondment decreased with increasing thickness and Cr (III) oxide content of the Cr (III) derived coating. Disbondment kinetics are explained in terms of coating porosity, chemical composition and electrocatalytic activity of the various metallic surfaces for the cathodic oxygen reduction reaction (ORR). Diminished electrocatalytic activity for ORR, as determined from cathodic polarisation measurements with a rotating disk electrode, are found to correlate with diminished delamination kinetics.

1. Introduction

Trivalent chromium metal-oxide-carbide coatings for steel (Cr (III) coatings) are currently being developed within the steel industry as a potential chromate-free replacement for Electro Chromium Coated Steel (ECCS). ECCS is used in packaging applications and typically comprises of a low gauge (0.25 – 0.35 mm) plain carbon strip steel with a nanometric (~15 nm) duplex chromium coating consisting of a crystalline metallic chromium base layer overcoated with a chromium oxide layer [1,2]. ECCS is manufactured by a process of cathodic electrodeposition.

The ECCS electrodeposition electrolyte contains hexavalent chromium (chromate) and use of chromate based manufacturing processes will become restricted due to incoming European REACH regulations [3–9]. Consequently, there has been significant pressure on packaging steel producers to develop a chromate-free alternative to ECCS [2]. The food packaging industry has stated that any ECCS replacement must be non-toxic and possess corrosion resistance that is comparable to ECCS.

A chromate-free alternative based on a Cr(III) metal-oxide-carbide coating is currently under development [2,10–12]. Fundamental work underpinning the electrodeposition of such Cr (III) based coatings, using a rotating cylinder electrode, has previously been published by Wijenberg et al. [2]. However, the novel work presented here investigates Cr (III) coatings that have been produced on an industrial scale pilot coating line.

In contrast to ECCS, the Cr (III) coatings contain Cr (III) carbide in addition to Cr(III) oxide, due to decomposition of the formate-based electrolyte [2,11]. Formate ($HCOO^-$) is included in the electrolyte to destabilise the $Cr(H_2O)_6^{3+}$ complex and facilitate electrodeposition of chromium onto the steel substrate [2,11]. A full explanation of the proposed deposition process for the Cr (III) is described in depth by Wijenberg et al. [2].

Cr (III) oxide electrodeposits, such as ECCS, provide good corrosion resistance when used in conjunction with an organic overcoat [13]. As such, they are always used in conjunction with, for example, an epoxy phenolic lacquer (EP) or Poly(Ethylene) Tetraphthalate (PET) laminate system on both sides of the can wall [13–16]. One important failure mechanism for organically coated metals is corrosion-driven cathodic disbondment, Fig. 1, where a loss of adhesion between the metal/polymer interface occurs, which is associated with cathodic oxygen reduction [17–25]. This corrosion mechanism is relevant in situations where oxygen is present such as, the outside of the can wall and inside the can where residual oxygen can be present initially.

In the current study, SKP experiments were carried out on iron and Cr (III) coated steel, of varying Cr coating thickness and composition, in high humidity (93% R.H.) air where 0.86 M $NaCl_{(aq)}$ was added to a penetrating defect. By studying the delamination of the PVB overcoat on a range of Cr (III) coated steels, it was possible to evaluate the rate and time dependent order of cathodic delamination kinetics.

Subsequently, the potential mechanisms of corrosion-driven cathodic disbondment of the PVB overcoat from Cr (III) coated steel substrates are evaluated. Finally, electrocatalytic activity for cathodic

E-mail address: 554907@swansea.ac.uk (J.E. Edy).

https://doi.org/10.1016/j.corsci.2019.04.037
Received 14 January 2019; Received in revised form 20 April 2019; Accepted 26 April 2019
Available online 30 April 2019

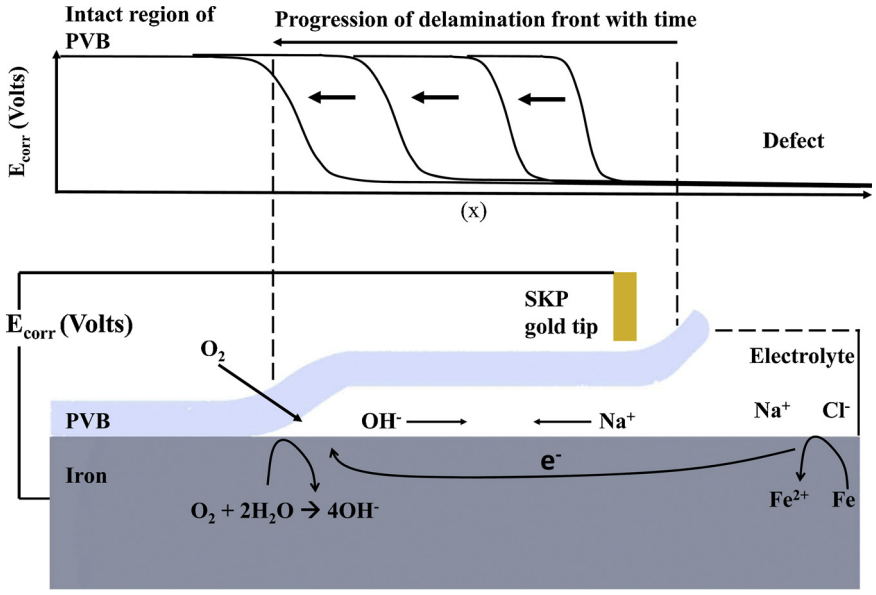

Fig. 1. Schematic representation of the corrosion-driven delamination cell showing correspondence to various regions of the time-dependent $E_{corr}(x)$ profile.

oxygen reduction is shown by cathodic polarisation plots, obtained using a rotating disc electrode (RDE), for iron, chromium, ECCS and Cr (III) coated steel.

2. Materials and methods

2.1. Materials

Iron foil (99.5% purity) and chromium foil (99.99% purity) were purchased from Goodfellow Cambridge Ltd. All samples of ECCS and Cr (III) coated steel were donated by TATA Steel Packaging Europe. All chemicals used were analytical grade quality and were obtained from Aldrich Chemical Company.

2.2. Methods

Cr (III) coatings of varying coating thicknesses were electroplated onto strip steel using an industrial scale pilot coating line at Tata steel Europe. Coatings of varying thickness and composition were achieved by varying the applied plating current at a fixed line speed. The chemical composition of chromium coatings of ECCS and Cr (III) coated steels were characterised by X-ray Photoelectron Spectroscopy (XPS) and X-ray fluorescence (XRF).

X-ray Photoelectron Spectroscopy (XPS) spectra and depth profiles were recorded on a Kratos Axis Ultra using monochromated Al Kα X-rays of 1486.8 eV. The measured spot size was 700 µm x 300 µm. Depth profiles were recorded using 4 KeV Ar^+ ions to create a sputter crater of 3 mm x 3 mm. Sputter rate was calibrated against XRF results and was 1.59 nm min^{-1}.

XPS depth profile spectra representative of ECCS and Cr (III) coated steel is shown in Fig. 2(a) and (b) respectively. Chemical compositions of ECCS and the Cr (III) coated steel substrates tested here are also listed in Table 1.

Surface images were obtained using a JEOL 7800 Field Emission Gun Scanning Electron Microscope. Unless explicitly stated in the figures, SEM images were obtained using an accelerating voltage of 7 kV and working distance of 8.1 mm.

The use of the Scanning Kelvin Probe (SKP) apparatus for study of corrosion-driven disbondment has been described extensively elsewhere [20,26,27]. Delamination test cells were prepared according to the work presented by Stratmann et al. [20,26,28]. Polyvinyl Butyral (PVB) solutions MW 70,000–100,000 were prepared in ethanol (15.5% w/w).

Iron and chromium samples were abraded by hand using silicon carbide paper and polished using an aqueous slurry of 5 µm alumina to remove any surface contaminants and a pre-existing oxide layer. ECCS and Cr (III) coated steel samples were not abraded or polished to avoid removing the nanometric chromium coating from these materials. Degreasing was carried out via an acetone rinse followed by air-drying. PVB solution was then bar cast onto a pre-cleaned sample and left to air dry. Insulating electrical tape was applied to the sample before bar casting of PVB to provide height guides to produce an air-dried thickness of 30 µm. Following this, tape was partially removed to create a 20 × 30 mm electrolyte reservoir (defect site).

All SKP delamination experiments were carried out in an enclosed SKP chamber maintained at 95% RH and 25 °C. The SKP apparatus used here has been described in detail elsewhere, as has the procedure for calibrating the SKP in terms of local free corrosion potential (E_{corr}) [29,30]. Frequent calibration checks were performed using a Cu/Cu^{2+} redox couple according to methodology described elsewhere [30]. Following the calibration procedure, it was found that for a bare metal surface corroding beneath an electrolyte film that,

$$E_{corr} = \Delta\psi_{Sol}^{Ref} + 0.555V \text{ vs. SHE} \quad (1)$$

Where SHE is the saturated hydrogen electrode and $\Delta\psi_{Sol}^{Ref}$ is the Volta potential difference measured between the SKP reference probe and the solution/air interface. Similarly, it was shown that for a metal surface covered with an adherent PVB film or with a PVB film which has become delaminated through the ingress of a thin electrolyte film.

$$E_{corr} = \Delta\psi_{Sol}^{Ref} + 0.330V \text{ vs. SHE} \quad (2)$$

Where $\Delta\psi_{Sol}^{Ref}$ is the Volta potential difference measured between the SKP reference probe and the polymer/air interface.

Delamination was initiated by introducing ~2 cm^3 of 0.86 M aqueous NaCl (pH 7) into the penetrative coating defect site. The SKP reference probe was positioned 12 mm away from the electrolyte reservoir (defect site) and instructed to scan towards and perpendicular to the defect site, Fig. 1. The SKP reference probe was a thin gold wire with a diameter of 125 µm, vibrated at 280 Hz with an amplitude of 40 µm. Kelvin probe potentials (E_{KP}) were measured at 20 points per mm. The height of the kelvin probe was controlled simply by a careful levelling of the sample and establishing the desired probe-sample distance at the beginning of the experiment. Since only minimal changes in the sample profile occur during delamination, due to ingress of the

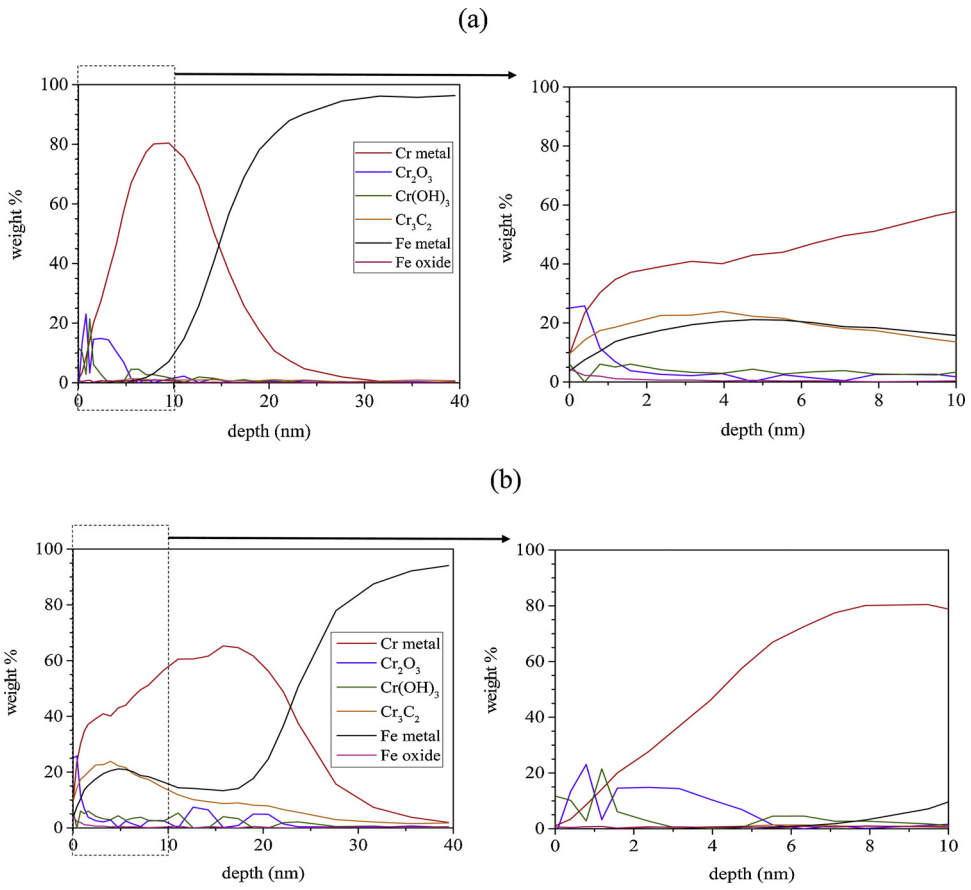

Fig. 2. XPS depth profile of (a) Electro chromium coated steel (ECCS) and (b) Cr (III) coated steel. The depth profiles on the left-hand side show the entire layer (up to 40 nm depth), whilst the inserted profiles on the right-hand side show the uppermost 10 nm of the ECCS (a) and Cr (III) coating, respectively. With reference to Table 1, the samples shown here are ECCS (sample E1) and Cr (III) coated steel (sample T6).

Table 1
Chemical composition (mg. m^{-2}) of ECCS and Cr (III) coated steel from XPS.

Chromium coating type	Sample Code	(mg. m^{-2}) Total Chromium	Chromium metal	Chromium hydr(oxide)	Chromium Carbide
ECCS	E1	93.4	82.1	9.3	2.0
Cr (III) coated steel	T1	57.9	32	18.2	6.7
	T2	58.4	36.3	4.2	12.9
	T3	61	45	4	12.0
	T4	80.5	57.9	6.8	15.8
	T5	94	69.9	13.3	11.1
	T6	134	102	8.2	23.8
	T7	156	112	25	19.0
	T8	167	122	20	25.0
	T9	205	153	31	21.0

electrolyte layer under the PVB film (approx. 5 μm), the probe height remains effectively constant [20,31].

An indirect measure of the change in E_{corr} between the intact metal-polymer interface and delaminated region, where ingress of electrolyte has occurred, was obtained using the SKP [18,20,21,32]. Distinct time-dependent E_{corr} profiles, Fig. 4, as detected by the SKP, develop as cathodic delamination advances away from the defect site.

For potentiodynamic studies of oxygen reduction on iron and chromium, ECCS and Cr (III) coated steel, circular samples of 22 mm diameter were punched from the various iron/ steel samples. Prior to this, the pure iron and pure chromium samples were abraded using 360, 600, 1000 and 1200 grit silicon carbide grinding paper and subsequently polished using a 5 μm alumina aqueous slurry. ECCS and Cr (III) coated steel samples were not subject to abrasion or polishing to avoid removing the nanometric chromium oxide coating. All samples were degreased and cleaned by rinsing in ethanol, acetone and finally distilled water, after which they were air dried.

All electrochemical measurements were obtained in 0.5 M aqueous sodium sulphate (Na_2SO_4) containing 0.025 M sodium tetraborate ($Na_2B_4O_7.10H_2O$) and 0.1 M sodium hydroxide (NaOH), which gave a buffered solution of pH9.3. At this pH iron and chromium are both passive and so significant rates of metal corrosion are not expected. Samples were held within the PTFE holder of an Oxford Instruments RDE-2 rotating disk electrode instrument, supplied by Sycopel Scientific Instruments. A platinum gauze counter electrode and Gamry mercury/ mercury sulphate reference electrode was used in a standard 3-electrode cell configuration.

In the case of pure iron and chromium, prior to each experiment, the working electrode was held at a potential just above the onset of hydrogen evolution (-1.2 V vs SHE) to reduce any air formed oxide film. Quasi-steady state anodic-going polarisation curves were obtained using a linear scan rate of 3.3×10^{-4} $V.s^{-1}$ following a methodology used elsewhere [17,33]. The initial applied potential used was -1.2 V vs SHE and was swept in the anodic direction towards the open circuit potential of the sample. A fixed rotation speed of 217 rad s^{-1} was chosen as it gave an optimum signal to noise ratio.

3. Results and discussion

3.1. XPS Characterisation of chromium coatings on steel

Composition vs. depth profiles obtained using X-ray photoelectron spectroscopy (XPS) for ECCS and typical Cr (III) coatings are given in Fig. 2a and b, respectively. Fig. 2a shows that, in the case of ECCS, chromium (III) oxide (Cr_2O_3) is most abundant in the outermost ~5 nm of a 20 nm coating. Similarly, the highest concentrations of chromium (III) hydroxide ($Cr(OH)_3$) are found in the outermost ~3 nm, although some subsurface $Cr(OH)_3$ is detected at 6–7 nm. Fig. 2b shows that, in

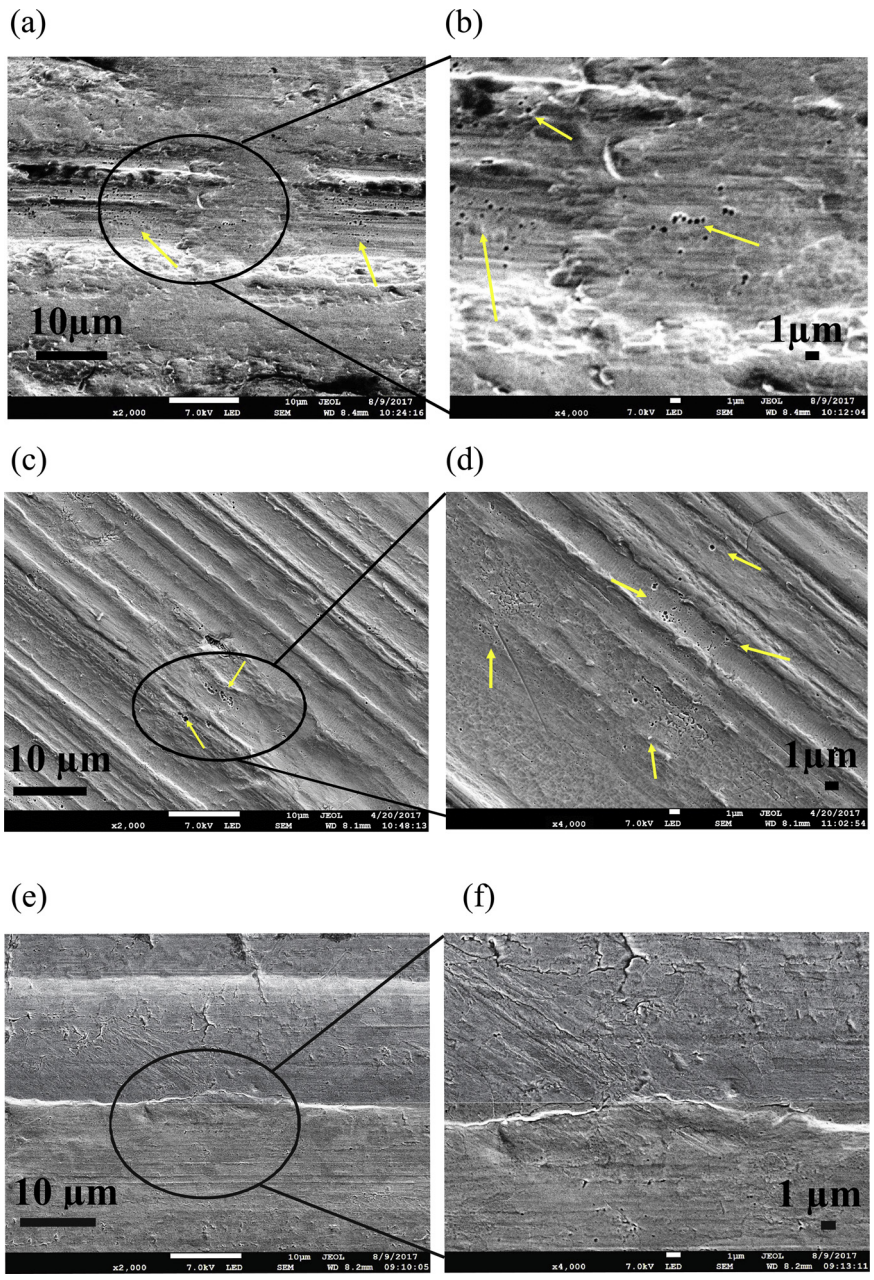

Fig. 3. Surface overview of chromium coated steel. (a) low thickness Cr (III) coated steel (T1) showing high density of surface defects (pores) (b) high thickness Cr (III) coated steel (T5) –showing a lower population of surface defects (pores), (c) ECCS surface (E1) – showing no evidence of pores.

the case of Cr (III) coated steel, Cr_2O_3 is again most abundant in the outermost ~2 nm of a 30 nm coating. However, in contrast with ECCS both Cr_2O_3 and Cr $(OH)_3$ are found throughout the full thickness of the coating. Furthermore, and again in contrast with ECCS, Fig. 2b shows that chromium (III) carbide (Cr_3C_2) is abundant throughout the Cr (III) derived coating present on Cr (III) coated steel.

Table 1 shows the depth-averaged chemical composition of ECCS and various Cr (III) coatings obtained by numerical integration of XPS data like that given in Fig. 2. In Table 1 chromium (III) oxide and hydroxide are combined as chromium (III) (hydr)oxide. It may be seen from Table 1 that whereas ECCS contains very little Cr_3C_2 all the Cr (III) coatings contain significant amounts of Cr_3C_2. Furthermore, the Cr (III) coatings contain variable amounts of chromium metal and chromium (III) (hydr)oxide and, in some cases, the chromium oxide:metal ratio for Cr (III) coated steel is much higher than is the case for ECCS.

3.2. SEM characterisation of Cr (III) coated steel and ECCS surfaces

Characterisation of the Cr (III) coated steel and ECCS surfaces were carried out using a JEOL 7800 FEG-SEM. Fig. 3(a) and (c) show low magnification SEM images of low coating weight (sample T1) and high coating weight (sample T6) Cr (III) coated steel samples, respectively. These images show coarse parallel striations, spaced 1–10 µm apart, which correspond to the surface roughness of the underlying cold rolled steel substrate. In addition, small sub-micron circular pores can be seen across the surface associated with the Cr (III) coating itself. These pores can be seen more clearly in the high magnification insert images, Fig. 3(b) and (d), respectively.

Fig. 3(e) shows a low magnification image of the ECCS surface (sample E1). The same coarse parallel striations are visible as in the case of the Cr (III) coating samples. However, there is no evidence of any porosity in the ECCS coating.

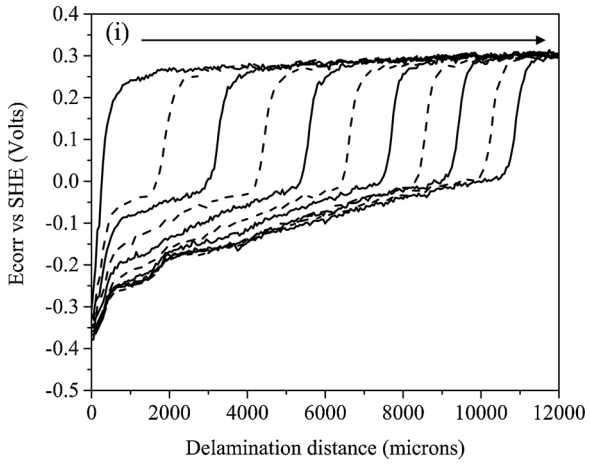

Fig. 4. SKP derived E_{corr} vs. distance from defect (x) profiles for a 30_{um} PVB film on a clean iron surface in 93% R.H. air. Scan times = (i) 60 min and 1-hour intervals thereafter.

The defects (pores) observed in the Cr (III) coating surface are similar to those observed previously for Cr (III) metal-oxide-carbide coatings [16]. These defects are thought to arise as a result of hydrogen evolution occurring at the strip surface during cathodic electrodeposition of the Cr (III) coating [2]. Moreover, it has previously been proposed that deposition of Cr (III) coating is blocked at sites on the steel surface at which hydrogen is being evolved and is reasonable to suggest that this would lead to increased steel exposure through the Cr (III) coating and a reduction in corrosion performance [2].

3.3. SKP studies of cathodic delamination kinetics

Cathodic disbondment kinetics of the PVB coating on iron were measured to obtain a reference point for cathodic delamination of the PVB overcoat in the absence of a chromium coating. Corrosion was seen to initiate on iron within one hour of the 0.86 mol. dm^{-3} $NaCl_{(aq)}$ electrolyte being added to the PVB coating defect. As delamination proceeded, distinctive time-dependent $E_{corr}(x)$ vs. distance profiles, as shown in Fig. 4, were detected by the SKP in line with studies on iron presented elsewhere [16,23,30].

The time-dependent $E_{corr}(x)$ profiles for iron and Cr (III) coated steel, Figs.4–5(a) and (b) respectively, develop due to ionic current flux passing along the thin layer of electrolyte that ingresses beneath the delaminated coating that produces an ohmic potential gradient linking the anodic coating defect site, Eq. (3), to the site of cathodic oxygen reduction, Eq. (4), at the coating delamination front [34,35].

In Fig. 4, a sharp potential drop of ca. 0.3 V may be seen in the immediate vicinity of the delamination front. Subsequently, an approximately linear, more gradual, potential drop links to delamination front to the region next to the coating defect, where potentials fall to c.a. -0.4 V.

$$Fe \rightarrow Fe^{2+} + 2e^{-} \quad (3)$$

$$O_2 + 2H_2O + 4e^{-} \rightarrow 4OH^{-} \quad (4)$$

Delamination kinetics of Cr (III) coated steel, of varying Cr (III) metal-oxide-carbide coating thickness and composition, overcoated with the model PVB polymer film were determined using the same methodology for iron. ECCS has previously been shown to be highly resistant to corrosion-driven cathodic disbondment and is not studied further here [16].

In contrast, corrosion initiated on Cr (III) coated steel within 1–2 hrs of the 0.86 mol. dm^{-3} $NaCl_{(aq)}$ electrolyte being added to the external coating defect site. Widespread anodic dissolution and deposition of corrosion product was observed in the external coating defect site,

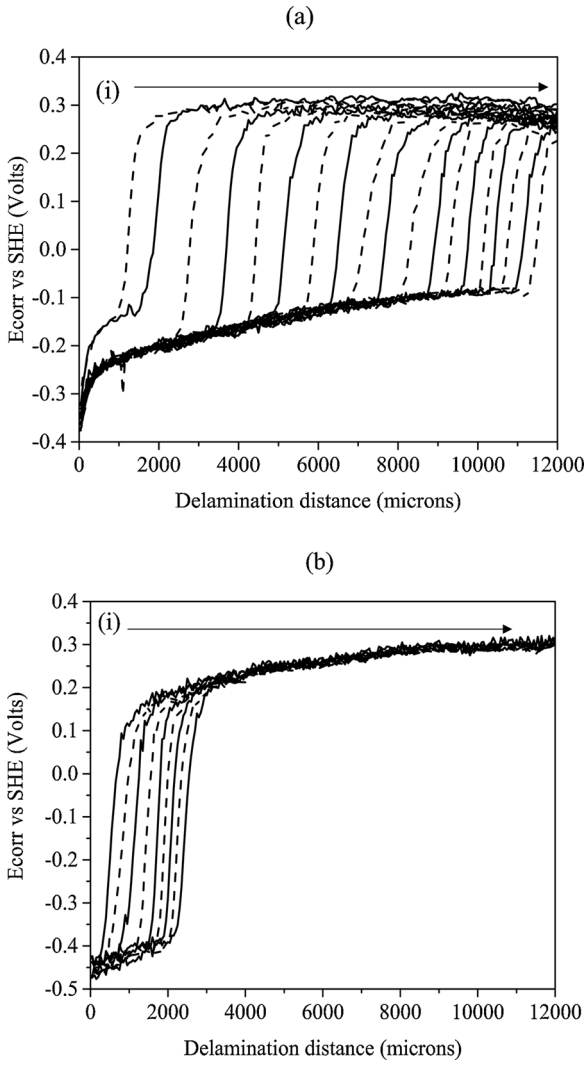

Fig. 5. A Typical SKP derived E_{corr} vs. distance from defect (x) profile for Cr (III) coated steel overcoated with a 30_{um} PVB film in 93% R.H. air (a) A Cr (III) coated steel demonstrating parabolic cathodic delamination kinetics, (b) A Cr (III) coated steel demonstrating linear cathodic delamination kinetics. Scan times for (a) = (i) 2430 min and 2-hour intervals thereafter. Scan times for (b) = (i) 2430 min and 4-hour intervals thereafter.

within 1 h of electrolyte introduction. Consequently, there is no reason to believe that the Cr (III) coating in the defect region inhibits anodic iron dissolution to the extent that this might influence the coupled kinetics of cathodic delamination. Typical $E_{corr}(x)$ profiles for low coating weight (poorer performing) Cr (III) coated steels and high coating weight (better performing) Cr (III) coated steel substrates are shown in Fig. 5(a) and (b), respectively.

The position of the cathodic delamination front is taken as the midpoint of the sharp drop in potential from the intact coating region, as has been described elsewhere [18,20,21,26,28]. Fig. 6 shows the distance from the coating defect to the delamination front (χ_{del}) plotted versus the SKP scan time minus the time taken for corrosion-driven delamination to become initiated ($t_{del} - t_i$). Delamination kinetics for the PVB overcoat on iron and lower coating weight Cr (III) (samples T1 – T3), can be seen in Fig. 6, and are found to be substantially parabolic in nature.

Parabolic kinetics are consistent with the delamination rate being controlled by the underfilm migration of electrolyte derived cations (Na^+ here) between the anode (defect) and cathode (delamination front) [16,18,20]. Under these circumstances, the delamination

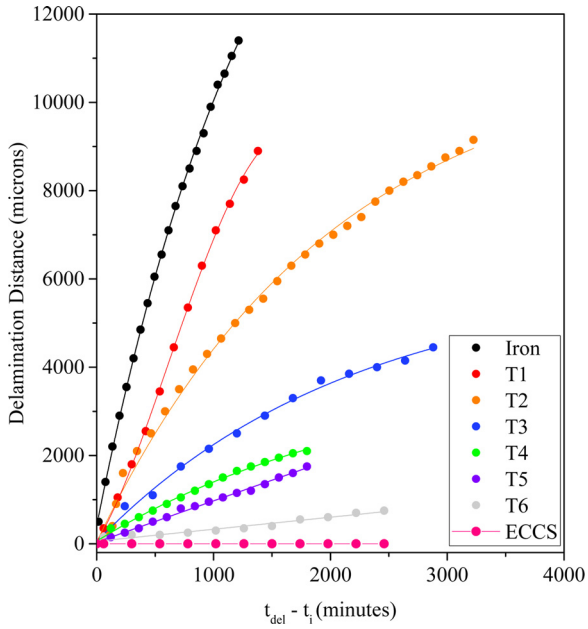

Fig. 6. Delamination distance (X_{del}) vs. time for (a) iron and Cr (III) coated steel variants (T1 – T6).

distance (χ_{del}) is related to time according to Eq. (5), where k_d is the parabolic rate constant and t_i is the initiation period.

$$\chi_{del} = k_d \cdot (t_{del} - t_i)^{1/2} \quad (5)$$

However, in the case of the higher coating weight Cr (III) coated steel samples T5 – T6, also shown in Fig. 6, the delamination kinetics are substantially linear with respect to time (χ_{del} increases linearly with time). This finding is not consistent with rate control by underfilm Na^+ migration. Conversely, it would be consistent with rate control by a (vertical) interfacial process such as electron transfer associated with the cathodic oxygen reduction reaction at the cathodic delamination front [18,20].

The extent to which the various delamination kinetics, shown in Fig. 6, approximate to either a parabolic or a linear rate is quantified in Table 2. Table 2 lists the R^2 correlation coefficient values obtained when χ_{del} vs ($t_{del} - t_i$) data sets are fitted to either Eq. (5) or to a straight line using least-squares regression [36]. It may be seen that for iron and the low coating weight (T1 – T3) Cr (III) coated steel samples, that the parabolic R^2 values are > linear R^2 values. Conversely, for the high coating weight (T5 and T6) samples, the linear R^2 values are > parabolic R^2 values. For the intermediate T4 Cr (III) coated steel sample, the parabolic R^2 value is approximately equal to the linear R^2 value, indicating mixed kinetics.

3.4. Effect of Cr (III) coating thickness and composition on cathodic disbondment rate

Since the kinetics of cathodic disbondment vary between parabolic in the case of iron and low coating weight Cr (III) coated steel, to linear on higher coating weight Cr (III) coated steel, the initial rate of PVB disbondment was used as the measure of comparison between the various samples. Initial rates $(d\chi_{del}/dt)_{initial}$ were estimated by constructing a tangent to the individual χ_{del} vs ($t_{del} - t_i$) curves, shown in Fig. 6, at ($t_{del} - t_i$) = zero and determining the gradient of that tangent.

The values of $dx_{del}/dt_{initial}$ thus obtained are plotted in Fig. 7 versus the various Cr (III) coating weight components resolved in terms of a) metallic chromium, b) chromium oxide, c) chromium carbide, and d) total chromium. Various simple mathematical functions were used, in an attempt, to fit the data shown in Fig. 7 and the best fit, at least in the case of chromium metal, Fig. (7)(a), and total chromium, Fig. 7(d), was obtained using an exponential decay, Eq. (6):

$$d\chi_{del}/dt = (d\chi_{del}/dt)_{initial} \cdot \exp^{-\left(\frac{x}{c}\right)} \quad (6)$$

where $(d\chi_{del}/dt)_{initial}$ is the rate where x = zero, x is the relevant coating weight component ($mg.m^{-2}$) and c is an adjustable variable. The best fit to Eq. (6) is plotted as the solid curve in Figs. 7(a)–(d) and the associated correlation coefficients are listed in Table 3.

It may be seen from Fig. 7 that the initial rate of PVB cathodic delamination decreases with increasing Cr (III) coating weight. This effect is most clearly seen in relation to the total chromium content, Fig. 7(d), where the amount of scatter in the data is minimal and the correlation coefficient associated with the fit to Eq. (6) is 0.78.

In contrast, the data derived for chromium carbide, Fig. 7(c), is highly scattered and the associated correlation coefficient is very low (R^2 = 0.06). The data sets derived for the chromium metal, Fig. 7(a), and chromium oxide, Fig. 7(b), components of the Cr (III) coatings show intermediate amounts of scatter and correspondingly intermediate correlation coefficients of 0.63 and 0.75, respectively.

Based on the above there is no reason to propose that chromium carbide contributes significantly to the cathodic disbondment resistance associated with the Cr (III) coatings. Conversely, it would seem reasonable to propose that the chromium metal and chromium oxide components of the Cr (III) coating do contribute. However, the similar degree of scatter and similar correlation coefficients associated with the chromium metal, Fig. 7(a), and chromium oxide, Fig. 7(b), data sets do not allow us to state with any certainty which of these coating components exerts the dominant effect.

It would be tempting to interpret the exponential relationship, Eq. (6), mechanistically, for example by proposing that the Cr (III) coating increases the overpotential for cathodic oxygen reduction in a manner proportional to the Cr (III) coating weight. Such a proposition is in fact consistent with the polarisation data shown in Fig. 8 and 9, discussed later. However, such an interpretation would only be rational if activation controlled cathodic oxygen reduction was only and always the rate determining process in PVB delamination on Cr (III) coated steel.

This is not immediately consistent with the parabolic (Na^+

Table 2
R^2 values for parabolic and linear fits of delamination kinetics on iron and Cr (III) coated steel samples. Corresponding kinetic plots are shown in Fig. 6(a)–(b).

			Correlation Coefficient		
	Figure	Sample	Parabolic	Linear	
Increasing Cr (III) coating weight ↓	6	Fe	0.995	0.984	
		T1	0.995	0.987	Substantially parabolic
		T2	0.991	0.966	
		T3	0.990	0.965	
		T4	0.979	0.976	Mixed
		T5	0.929	0.996	Substantially linear
		T6	0.898	0.964	

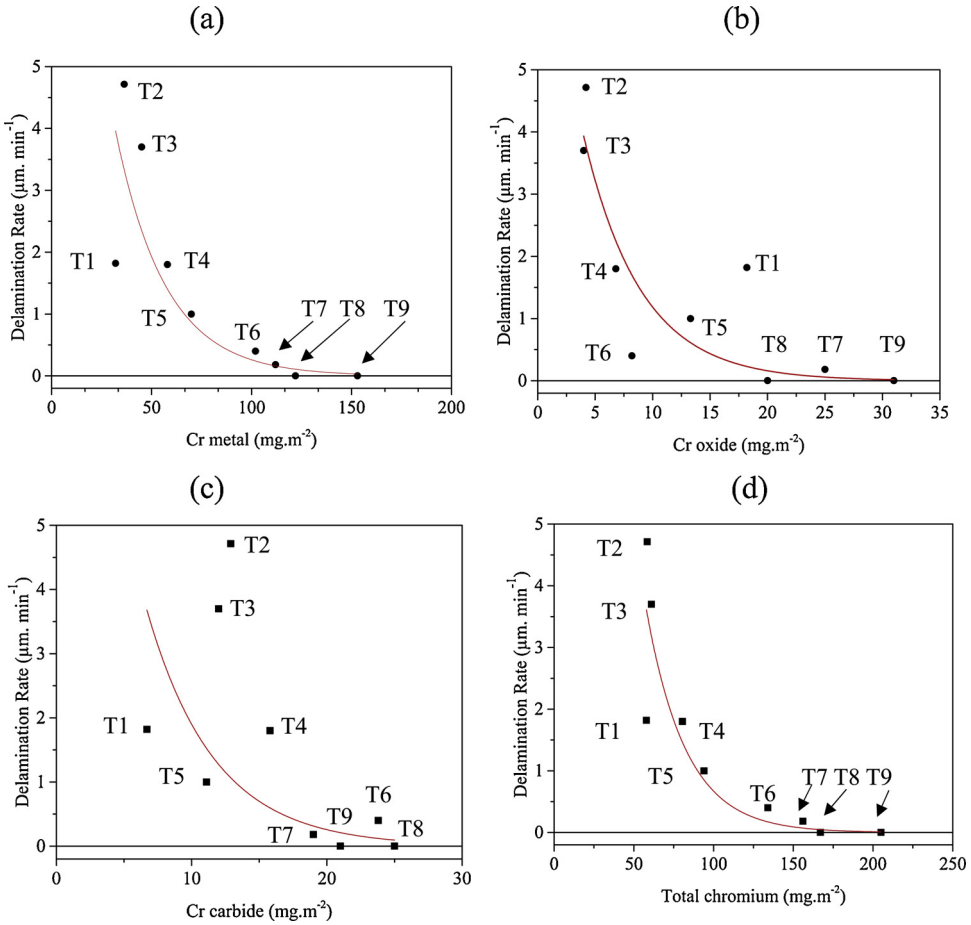

Fig. 7. Cathodic delamination rate (µm. min^{-1}) plotted against the coating parameters of Cr (III) coated steel (mg. m^{-2}): (a) chromium metal (b) chromium oxide (c) chromium carbide (d) total chromium. Codes on figure correspond to those listed in Table 1.

Table 3
R^2 values for $dx_{del}/ dt_{initial}$ versus various Cr (III) coating components, Fig. 7(a)–(d) fitted according to the exponential decay fit, Eq. (6).

Coating component	Figure	Correlation Coefficient (R^2)
chromium metal	7(a)	0.63
chromium oxide	7(b)	0.75
chromium carbide	7(c)	−0.06
chromium total	7(d)	0.78

migration controlled) delamination kinetics seen for the lower Cr (III) coating weights (samples T1 – T4). Possibly, the two notions could be reconciled by assuming that the initial rate of disbondment (before a significant cation migration pathlength, χ_{del}, develops) is always activation controlled. However, such a proposition is necessarily speculative and would require further work to confirm.

The observation of parabolic delamination kinetics on iron and low coating weight Cr (III) coated steel (T1- T3) and the change to linear (zero order) delamination kinetics on higher coating weight Cr (III) coated steel (T5- T6) suggests that a reduction in cathodic electron transfer rate may result as the overall thickness of the Cr (III) coating increases above 125 mg.m-2. These higher coating weight Cr (III) variants (T5 – T6) are also associated with elevated levels of chromium (III) oxide (> 8 mg.m^{-2}). Given the relatively poor electrical conductivity of chromium (III) oxide, it is possible that Cr (III) coatings with sufficient oxide content could be capable of resistively inhibiting electron transfer rate [42] to the point that this becomes the rate determining process in cathodic delamination. We can eliminate diffusional mass transport of O_2 through the PVB coating as a rate

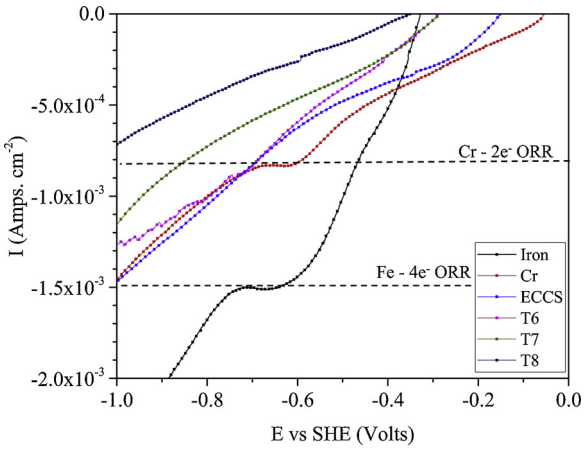

Fig. 8. Anodic going quasi-steady state potentiodynamic cathodic polarisation curves for (a) iron, chromium metal, and Cr coated sample E1, and Cr (III) coated steel variants T6-T8. Scan rate of 3.3 × 10^{-4} V.s^{-1}. Scan range -1.2 V vs SHE to OCP. Fixed RDE rotation of 217 radians s^{-1}.

determining process as this has been shown to only be important for organic coatings loaded with diffusion blocking additives and/or pigments [35], and is not the case in our studies here for unpigmented PVB coatings on iron and Cr (III) coated steel.

Regarding the actual mechanism of coating disbondment, various such mechanisms have been proposed elsewhere, including: i) alkaline hydrolysis of a pre-existing oxide layer at the metal-polymer interface [27], ii) reaction of the alkaline electrolyte directly with the polymer

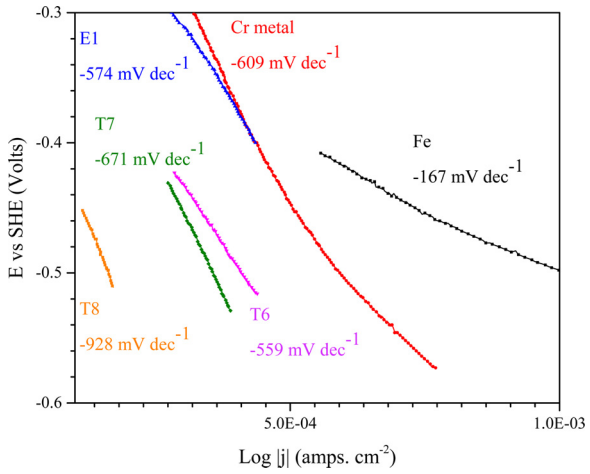

Fig. 9. Tafel plots of iron and pure chromium foil, sample E1, and Cr (III) coated steel variants T6 – T8.

bonds, iii) oxidation of the polymer by reactive intermediates associated with the cathodic oxygen reduction reaction (Eq. (2)). and iv) physical displacement of the coating at the metal-polymer interface by the alkaline electrolyte.

In considering these possibilities: It has been shown that alkaline dissolution of the oxide layer at the metal-polymer interface is not a significant disbondment mechanism for iron [27,36]. Although, hydrogen peroxide (H_2O_2) is a product of the 2 electron cathodic reduction of dioxygen and that various peroxy species can occur as reactive intermediates in the reduction process [17,18,26]. Thus, hydrogen peroxide could be expected to drive the oxidative dissolution of Cr (III) hydroxide to CrO_4^{2-} under alkaline conditions, similar to those prevailing in the underfilm environment during cathodic disbondment [18,37–39]. It is therefore also possible that oxidative dissolution of Cr (III) hydroxide might occur in our experiments and contribute to the inhibition of cathodic disbondment. We are not currently able to quantify the extent to which such a process does occur. However, it would seem reasonable to propose that any evolution of CrO_4^{2-} would be transient because CrO_4^{2-} could itself be reduced back to Cr (III) in the cathodic reaction.

Thermodynamic data indicates that the chromium (III) hydr(oxides) would themselves be sparingly soluble present in the alkaline conditions (pH 9–14) found at the disbondment front, [36,37]. However, Zydorczak et al., followed the kinetics of chromium (III) oxide dissolution in deaerated 1 M aqueous NaOH (pH14) and, after 10 days, measured a concentration less than 5 mM [38]. Given this fact, it remains unclear whether direct alkaline dissolution of chromium (III) oxide is a significant disbondment mechanism for the PVB overcoat on Cr (III) coated steel.

A loss of adhesion due to reaction between the alkaline electrolyte and polymer or polymer-substrate bond seems likely to be the most important disbondment mechanism given that the polymer used (PVB) is polyvinyl butyral-co-acetate-co-alcohol and acetate functions are prone to alkaline hydrolysis. However, we cannot rule out contributions due to reaction of PVB with free radical intermediates produced during cathodic oxygen reduction or, indeed, physical displacement. Disbondment by physical displacement of the coating by the alkaline electrolyte has been suggested previously by Evans [40]. The affinity for water of oxide-covered surfaces increases as pH moves further from the isoelectric point (pH point of zero charge (pzc)) of that oxide [41]. Given a pzc of 6.5–7.4 for chromium (III) oxide, a competitive displacement of the coating, at the disbondment front (pH14), could be expected.

3.5. Electrochemical characterisation of the Oxygen Reduction Reaction (ORR)

To evaluate whether Cr (III) oxide levels significantly influence the rate of ORR for ECCS and Cr (III) coatings a series of cathodic polarisation plots were obtained using rotating disc voltammetry. Fig. 8 shows a series of anodic going quasi-steady state polarisation curves for iron, chromium, E1 and T6 – T8 samples, detailed in Table 1, which were obtained as an assessment of their ability to support the cathodic oxygen reduction reaction (ORR) in aqueous sodium sulphate electrolyte buffered to pH 9.3.

The Cr (III) coating variants (T6 – T8) were selected for study because they all have similar chromium metal contents (102–122 mg m^{-2}) but widely varying chromium (III) oxide contents, 8.2 mg.m^{-2} for T6 and 20–25 mg m^{-2} for T7 and T8 respectively. They are also relatively thick coatings for which a significant change in polarisation characteristics, relative to iron, might be anticipated. Polarisation curves were obtained using a rotating disk electrode set to rotate at fixed angular velocity of 217 rad.s^{-1}, to minimise as much as possible, any mass transport limiting effect on measurable current density.

OCP values observed for Cr (III) coated surfaces and iron were found to be similar, whereas, OCP values for chromium metal and ECCS (E1) were slightly anodic relative to iron and Cr (III) coatings. The more positive OCP observed for chromium metal and ECCS may be explained by an increased inhibition of the anodic process on these materials compared to Cr (III) coatings. Similarly, the similarity of OCP values for Cr (III) coatings and iron may be explained by an increase in the anodic process, possibly due to a degree of iron contamination in the Cr (III) coating layer resulting from the cathodic electrodeposition process for Cr (III) coated steel.

Fig. 8 shows the cathodic polarisation curve for iron, chromium, ECCS and Cr (III) coated steel (samples E1 and T6-T9). A diffusion limited and potential independent plateau of current density of 1.5×10^{-3} A.dm^{-2} at E = -0.66 V vs SHE for oxygen reduction was observed on iron, consistent with findings elsewhere [33,40,41]. The E–I polarisation curve for chromium metal also features a diffusion limited, potential independent, plateau at a significantly lower current density of 8.32×10^{-4} A.dm^{-2} at E = -0.66 V vs SHE.

It has been shown previously [42] that in weakly alkaline electrolytes and at potentials low enough to produce a bare iron surface that O_2 may be reduced to hydroxyl ions (OH^-) via a direct 4e- pathway, Eq. (7). Conversely, for oxide covered surfaces ORR may proceed via a 2e- pathway with the formation of hydroxyl ions and hydrogen peroxide, Eq. (8). However, hydrogen peroxide may become oxidised by the reaction, shown in Eq. (9). It is therefore possible to observe $4e^-$ and $2e^-$ pathways both separately and in a number of combinations [43].

$$O_2 + 2H_2O + 4e^- \rightarrow 4OH^- \quad (7)$$

$$O_2 + 2e^- + 2H_2O \rightarrow 2OH^- + H_2O_2 \quad (8)$$

$$HO_2^- + H_2O + 2e^- \rightarrow 3OH^- \quad (9)$$

The theoretical number of electrons transferred during ORR for the iron and chromium metal surfaces studied here can be calculated using the Levich Equation, Eq. (10).

$$i_L = 0.62nFD^{2/3}v^{-1/6}c\omega^{1/2} \quad (10)$$

where i_L is the limiting current (obtained from Fig. 8), n is the number of electrons transferred per molecule of oxygen reduced, F is the Faraday constant (96,485 C. mol^{-1}), c (mol. cm^{-3}) the bulk concentration of dissolved oxygen, D is the oxygen diffusion coefficient ($cm^2\,s^{-1}$), v is the kinematic viscosity ($cm^2\,s^{-1}$) and ω is the angular velocity (217 rad s^{-1} here) [44]. Values of the coefficients in Eq. (10) were obtained from published data obtained at 20 °C, where D = 1.74 × 10^{-5} $cm^2\,s^{-1}$, v = 10^{-2} $cm^2\,s^{-1}$, c = 2 × 10^{-7} [45].

Using Eq. (10), the theoretical number of electrons transferred during ORR is 3.69 for iron and 1.84 for chromium metal, consistent with the lower current density observed in Fig. 8 for chromium metal. Thus, the difference in plateau current density between iron and chromium metal may be explained where ORR on the bare iron surface proceeds predominantly via the $4e^-$ O_2 pathway, Eq. (7), but proceeds on the oxide covered chromium metal via the $2e^-$ pathway, Eq. (8). However, no current density plateau is observed for either ECCS or Cr (III) coated steels (samples E1 and T6 - T8) which indicates that the activity of these surfaces to support ORR is lower than the rate of diffusion of oxygen to the electrode surface. A reduction in measured current densities for ORR is observed as chromium metal and chromium (III) oxide content is increased in the Cr (III) coating (samples T6 – T8).

The kinetics of ORR, extensively discussed elsewhere [33,40,41,43,46], can be determined, where the overpotential is large, by plotting the applied potential against the logarithm of cathodic current to construct a Tafel slope. The slope is determined by parameters given in Eq. (11), where R is Universal Gas Constant, T is temperature in Kelvin, α_0 is the electron transfer coefficient, n_{a0} is the number of electrons transferred in the rate determining step and F is Faraday's constant. Thus, the higher the Tafel slope, the high the overpotential increases with increasing current density. Therefore, to obtain fast kinetics or a high current at a low overpotential, then the reaction should show a low Tafel slope or a large $\alpha_0 n_{a0}$.

$$\frac{2.303RT}{\alpha_0 n_{a0} F} \tag{11}$$

To calculate the kinetics of ORR, Tafel slopes were constructed using the portion of the E–I curve lying within the region of kinetic (or activation) control, where the cathodic reaction rate would be interfacial electron transfer limited rather than diffusion limited. Tafel slopes for Iron, pure chromium, ECCS and Cr (III) coated steel materials are shown in Fig. 9.

In the case of iron and chromium, which exhibited a diffusion limited current plateau, the Tafel slope was plotted using the kinetic current density (i_K) to minimise any influence of mass transport limitation. ORR has been demonstrated to be first order with respect to O_2 on iron previously and is assumed to be the case here for all the chromium materials tested in our study [40]. Under such a case, the disk current density (i) is equal to the sum of the kinetic current density (i_K) and the mass transport limiting current density (i_L) according to the Levich-Koutecky Eq. (12).

$$\frac{1}{i} = \frac{1}{i_k} + \frac{1}{i_L} \tag{12}$$

The Tafel slope calculated for iron, recorded in sodium sulphate buffered to pH 9.3, was -167 mV. dec^{-1}, similar to values obtained by Zečević et al. [41], who recorded a slope of -150mv dec^{-1} in borate buffered solution of pH9.8.

Mechanistic Tafel slopes for ORR usually have a slope of between 60 mV/dec^{-1} and 120 mV/dec^{-1} [41,46]. However, Tafel slopes for bare chromium metal, ECCS, and Cr (III) coated steel samples, Fig. 9, obtained here are much larger and so are not mechanistic. Instead, differences in ORR activity are explored by analysis of the surface-controlled region of the E–I polarisation curve, Fig. 8. Thus, to interpret ORR kinetics, linear regression of E–I polarisation curves, Fig. 8, for ECCS and Cr (III) coated steels (samples E1 and T6-T8), within the region of surface control was carried out. A strong linear dependence between potential and current density was found, with high correlation, R^2 values are reported in Table 4. The linearity between potential and current for ECCS and Cr (III) coated surfaces indicates the presence of resistive (ohmic) behaviour for these coatings. According to Ohm's law, Eq. (13), at a given current density, an increase in resistance will require an increase in voltage of equal magnitude to maintain the same current density.

Table 4
R^2 correlation coefficients for linear regression of E–I polarization curves and ohmic resistance values for each coating, calculated from E–I polarization curves.

Sample	E-I linear correlation (R^2) coefficient	R = V/I (Ohms)
Fe foil	0.984	500
Cr foil	0.995	747.889
E1	0.995	919.5402
T6	0.993	1184.51
T7	0.999	1362.468
T8	0.996	2564.103

$$V = I.R \tag{13}$$

Table 4 displays the calculated ohmic resistances of the materials tested here for ORR. As can be seen in Table 4, chromium shows. ca 25% higher resistivity relative to iron, suggesting that chromium is intrinsically less active. Further increases in ohmic resistance, can also be seen in Table 4, for the thicker and higher oxide containing chromium coatings (samples E1 and T6 – T8).

The ohmic behaviour of the Cr (III) oxide is consistent with the known wide band-gap semiconductor properties of Cr (III) oxide [47,48], and so it could be expected that interfacial electron transfer would be impaired on oxide covered electrode surfaces such as those present for Cr (III) coated steels. This then would be consistent with the reduced disbondment kinetics observed for thicker Cr (III) coatings associated with the diminished cathodic oxygen reduction measured by cathodic polarisation measurements.

A model for reduction processes on oxide covered films involving both charge transfer through the oxide film and charge transfer at the film-electrolyte interface has previously been proposed and may explain the effect of Cr (III) oxide content in Cr (III) coatings on ORR observed here [48–50]. The model proposes that electron transfer in ORR involves: (i) transfer of electrons over a potential barrier to an adsorbed oxygen molecule, where the rate is limited by the number of adsorbed oxygen molecules, number of electrons striking the film and the probability of electron transfer across it [49]. (ii) transfer of charge through the oxide film via electron tunnelling, possible where thin oxide films are transparent to electron tunnelling [49]. It was reported that the tunnelling current density, for a given potential bias, decreases sharply with increasing oxide thickness [49]. This may then explain the lower ORR currents measured for the thicker Cr (III) coatings here with elevated Cr (III) oxide content, where an increase in the proportion of applied potential is required to drive the tunnelling process due to thicker Cr (III) oxide, which in turn leads to diminished ORR activity. Indeed, Cr (III) coatings that demonstrate diminished ORR activity from cathodic polarisation measurements also show good resistance to corrosion-driven cathodic disbondment of the model PVB coating.

4. Conclusions

1 The rate of corrosion-driven disbondment of a model PVB coating are shown to decrease with increasing chromium (III) oxide content and total thickness of the Cr (III) coating. Thick Cr (III) coatings containing sufficient coating weights of Cr (III) oxide were found to resist corrosion-driven organic coating delamination such that they offered similar performance to that of ECCS.
2 Kinetics of cathodic disbondment on iron and low coating weight Cr (III) are rate-limited by the migration of Na^+ cations (parabolic). Whilst, a profound change from parabolic to linear (zero order) kinetics is observed for high coating weight Cr (III) coated steel variants (T5-T6).
3 Diminished O_2 reduction currents, as determined from cathodic polarisation measurements, are observed for the chromium-based materials relative to iron. Predominantly $2e^-$ ORR occurs on the oxide covered chromium surfaces and $4e^-$ ORR on the bare iron

electrode surface

4 A substantially linear relationship between potential and current is observed and a reduction in ORR currents with increasing Cr (III) oxide content of the ECCS and Cr (III) coated surfaces (samples E1 and T6 – T8) is also observed. Thus, it is proposed that ECCS and Cr (III) coatings may act as ohmic resistors, where coatings with higher Cr (III) oxide content demonstrate a larger resistivity and thus necessitate higher potentials to be applied in order to drive ORR at the surface.

5 Diminished electrocatalytic activity for ORR, as determined from cathodic polarisation measurements, are found to correlate with diminished delamination kinetics.

6 The thickness and Cr (III) content of Cr (III) coatings are both important for resisting corrosion-driven cathodic disbondment. Firstly, the overall thickness of the Cr (III) coating is important as to minimise the presence of defects (pores, pinholes) in the coating to ensure robust coverage of (act as a barrier to) the underlying (electrochemically active) steel substrate. Secondly, sufficient Cr (III) oxide in the Cr (III) coating is also necessary to effectively hinder interfacial electron transfer processes at the delamination front (cathode), to stifle ORR at the underfilm cathode and thus resist propagation of the delamination front.

7 The results here conclude that Cr (III) coatings are a possible replacement of ECCS for packaging applications with respect to their resistance to cathodic disbondment in aerated conditions.

5. Data availability statement

The raw/processed data required to reproduce these findings cannot be shared at this time as the data also forms part of an ongoing study.

Acknowledgements

The authors would like to thank TATA Steel and for financial support by EPSRC (EP/1015507/1) funded EDT MATTER (Manufacturing Advances Through Training Engineering Researchers) and the Materials and Manufacturing Academy (M2A). The work was further supported by the Advanced Imaging of Materials (AIM) Facility at Swansea University, funded in part by the EPSRC (EP/M028267/1), the European Regional Development Fund through the Welsh Government (80708) and the Ser Solar project via Welsh Government.

References

[1] I. Suzuki, Corrosion-resistant Coatings Technology, New York (1989).
[2] J.H.O.J. Wijenberg, M. Steegh, M.P.P. Aarnts, K.R.R. Lammers, J.M.C. Mol, Electrodeposition of mixed chromium metal-carbide-oxide coatings from a trivalent chromium-formate electrolyte without a buffering agent, Electrochim. Acta 173 (2015) 819–826 http://linkinghub.elsevier.com/retrieve/pii/S0013468615012608.
[3] D.M. Proctor, M. Suh, S.L. Campleman, C.M. Thompson, Assessment of the mode of action for hexavalent chromium-induced lung cancer following inhalation exposures, Toxicology. 325 (2014) 160–179, https://doi.org/10.1016/j.tox.2014.08.009.
[4] U.S. Environment Protection Agency, Toxicological Review of Hexvalent Chromium, (1998) http://www.epa.gov/iris.
[5] M. Peter, M. Neil, Factors affecting the reduction and absorption of hexavalent chromium in the gastrointestinal (GI) tract: potential impact on evaluating the carcinogenicity of ingested hexavalent chromium, Washington, D.C. (2012).
[6] S.S. Wise, C. Wise, H. Xie, L.J. Guillette, C. Zhu, J.P. Wise, J.P. Wise, Hexavalent chromium is cytotoxic and genotoxic to American alligator cells, Aquat. Toxicol. 171 (2016) 30–36.
[7] H.J. Gibb, P.S.J. Lees, P.F. Pinsky, B.C. Rooney, Lung cancer among workers in chromium chemical production, Am. J. Ind. Med. 38 (2000) 115–126, https://doi.org/10.1002/1097-0274.
[8] R.S. Luippold, K.A. Mundt, R.P. Austin, E. Liebig, J. Panko, C. Crump, K. Crump, D. Proctor, Lung cancer mortality among chromate production workers, Occup. Environ. Med. 60 (2003) 451–457 http://www.ncbi.nlm.nih.gov/pmc/articles/PMC1740552/pdf/v060p00451.pdf.
[9] B.C. Schneider, S.L. Constant, S.R. Patierno, R.A. Jurjus, S.M. Ceryak, Exposure to particulate hexavalent chromium exacerbates allergic asthma pathology, Toxicol. Appl. Pharmacol. 259 (2012) 38–44.
[10] M. Steegh, J. Wijenberg, Patent WO 2014 079910 A1.pdf, 2014.
[11] M. Steegh, J. Wijenberg, Patent WO 2014 079911 A2.pdf, 2014.
[12] J. Wijenberg, Passivation from trivalent chromium bath chemistry, MSc thesis, Utrecht University, NL, 2011.
[13] B. Boelen, H. Den Hartog, H. Van der Weijde, Product performance of polymer coated packaging steel, study of the mechanism of defect growth in cans, Prog. Org. Coatings. 50 (2004) 40–46.
[14] X. Zhang, B. Boelen, P. Beentjes, J.M.C. Mol, H. Terryn, J.H.W. de Wit, Influence of uniaxial deformation on the corrosion performance of pre-coated packaging steel, Prog. Org. Coatings. 60 (2007) 335–342.
[15] A.C. a De Vooys, B. Boelen, D.H. Van Der Weijde, Screening of coated metal packaging cans using EIS, Prog. Org. Coatings. 73 (2012) 202–210, https://doi.org/10.1016/j.porgcoat.2011.10.019.
[16] N. Wint, A.C.A. de Vooys, H.N. McMurray, The corrosion of chromium based coatings for packaging steel, Electrochim. Acta (2016) 1–11 http://linkinghub.elsevier.com/retrieve/pii/S0013468616301013.
[17] H. Dafydd, D.A. Worsley, H.N. McMurray, The kinetics and mechanism of cathodic oxygen reduction on zinc and zinc-aluminium alloy galvanized coatings, Corros. Sci. 47 (2005) 3006–3018.
[18] A. Leng, H. Streckel, M. Stratmann, The delamination of polymeric coatings from steel. Part 2: first stage of delamination, effect of type and concentration of cations on delamination, chemical analysis of the interface, Corros. Sci. 41 (1999) 579–597.
[19] G. Williams, H.N. McMurray, The mechanism of group (I) chloride initiated filiform corrosion on iron, Electrochem. Commun. 5 (2003) 871–877, https://doi.org/10.1016/j.elecom.2003.08.008.
[20] M. Stratmann, A. Leng, W. Fürbeth, H. Streckel, H. Gehmecker, K.H. Große-Brinkhaus, The scanning Kelvin probe; a new technique for the in situ analysis of the delamination of organic coatings, Prog. Org. Coatings 27 (1996) 261–267.
[21] A. Leng, H. Streckel, K. Hofmann, M. Stratmann, Part III: effect of oxygen partial pressure on delamination reaction, Corros. Sci. 41 (1999) 599–620.
[22] P.A. Sørensen, K. Dam-Johansen, C.E. Weinell, S. Kiil, Cathodic delamination: quantification of ionic transport rates along coating-steel interfaces, Prog. Org. Coatings. 68 (2010) 70–78.
[23] P.C. Dodds, G. Williams, J. Radcliffe, Chromate-free smart release corrosion inhibitive pigments containing cations, Prog. Org. Coatings. 102 (2016), https://doi.org/10.1016/j.porgcoat.2016.05.005.
[24] H. Bi, J. Sykes, Cathodic delamination of unpigmented and pigmented epoxy coatings from mild steel, Prog. Org. Coatings. 90 (2016) 114–125, https://doi.org/10.1016/j.porgcoat.2015.10.002.
[25] J. Sharman, J. Sykes, T. Handyside, Cathodic disbonding of chlorinated rubber coatings from steel, Corros. Sci. 35 (1993) 1375–1383.
[26] W. Fürbeth, M. Stratmann, Scanning Kelvinprobe investigations on the delamination of polymeric coatings from metallic surfaces, Prog. Org. Coatings. 39 (2000) 23–29, https://doi.org/10.1016/S0300-9440(00)00095-3.
[27] W. Fürbeth, M. Stratmann, The delamination of polymeric coatings from electrogalvanised steel – a mechanistic approach, Corros. Sci. 43 (2001) 207–227, https://doi.org/10.1016/S0010-938X(00)00047-0.
[28] A. Leng, H. Streckel, M. Stratmann, The delamination of polymeric coatings from steel. Part 1: calibration of the Kelvinprobe and basic delamination mechanism, Corros. Sci. 41 (1999) 547–578.
[29] G. Williams, H.N. McMurray, D.A. Worsley, Cerium(III) Inhibition of Corrosion-Driven Organic Coating Delamination Studied Using a Scanning Kelvin Probe Technique [Journal of The Electrochemical Society, 149, B154 (2002)], J. Electrochem. Soc. 149 (2002) L4, https://doi.org/10.1149/1.1479153.
[30] G. Williams, A. Gabriel, A. Cook, H.N. McMurray, Dopant effects in polyaniline inhibition of corrosion-driven organic coating cathodic delamination on Iron, J. Electrochem. Soc. 153 (2006) B425, https://doi.org/10.1149/1.2229280.
[31] G. Williams, H.N. Mcmurray, Chromate inhibition of corrosion-driven organic coating delamination studied using a scanning kelvin probe technique, J. Electrochem. Soc. 148 (2001) B377–B385, https://doi.org/10.1149/1.1396336.
[32] H.N. McMurray, G. Williams, Under film/coating corrosion, Shreir's Corros. (2010) 988–1004, https://doi.org/10.1016/B978-044452787-5.00040-8.
[33] N. Wint, S. Geary, H.N. McMurray, G. Williams, A.C.A. de Vooys, The kinetics and mechanism of atmospheric corrosion occurring on tin and iron-tin intermetallic coated steels, J. Electrochem. Soc. 162 (2015) C775–C784, https://doi.org/10.1149/2.0681514jes.
[34] G. Klimow, N. Fink, G. Grundmeier, Electrochemical studies of the inhibition of the cathodic delamination of organically coated galvanised steel by thin conversion films, Electrochim. Acta 53 (2007) 1291–1300.
[35] C.F. Glover, C.A.J. Richards, G. Williams, H.N. McMurray, Evaluation of multi-layered graphene nano-platelet composite coatings for corrosion control part II – cathodic delamination kinetics, Corros. Sci. 136 (2018) 304–310, https://doi.org/10.1016/j.corsci.2018.03.014.
[36] R.J. Freund, W.J. Wilson, Do.L. Mohr, Chapter 7 - linear regression, Stat. Methods, 3rd ed., Academic Press, New York, 2010, pp. 321–374.
[37] N. Krot, V. Shilov, A. Fedoseev, N. Budantseva, A. Yusov, A. YuGarnov, L. Charushmikova, V. Perminov, L. Astafurova, T. Lapiskaya, V. Makarenkov, Development of AIkaline Oxidative Dissolution Methods for Chromium (III) Compounds Present in Hanford Site Tank Sludges, Washington, D.C. (2000).
[38] M. Rock, B. James, G. Helz, Hydrogen peroxide effects on chromium oxidation state and solubility in four diverse, chromium-enriched soils, Environ. Sci. Technol. 35 (2001) 4054–4059, https://doi.org/10.1021/es010597y.
[39] G. Almerindo, A. Gaborim, L. Nicolazi, M. Idrees, F. Nome, H. Fiedler, R. Nome, Confocal fluorescence microscopy and kinetics of the Cr 3+ -Chromate ion oxidation equilibria at the solid liquid interface, J. Braz. Chem. Soc. 28 (2017) 1708–1714.

[40] V. Jovancicevic, The Mechanism of Oxygen Reduction on Iron in Neutral Solutions, J. Electrochem. Soc. 133 (1986) 1797, https://doi.org/10.1149/1.2109021.
[41] S. Zecevic, D.M. Drazic, S. Gojkovic, Oxygen reduction on iron: part III. An analysis of the rotating disk-ring electrode measurements in near neutral solutions, J. Electroanal. Chem. Lausanne (Lausanne) 265 (1989) 179–193.
[42] V. Jovancicevic, The Mechanism of Oxygen Reduction on Iron in Neutral Solutions, J. Electrochem. Soc. 133 (1986) 1797.
[43] H. Dafydd, D.A. Worsley, H.N. McMurray, The kinetics and mechanism of cathodic oxygen reduction on zinc and zinc-aluminium alloy galvanized coatings, Corros. Sci. 47 (2005) 3006–3018.
[44] A. Bard, G. Inzelt, F. Scholz, Electrochemical Dictionary, Springer Science and Business Media, 2012.
[45] V. Levich, Physiochemical Hydrodynamics, Prentice Hall Inc., Englewood Cliffs, NJ, 1962.
[46] C. Song, J. Zhang, Electrocatalytic oxygen reduction reaction, PEM fuel cell electrocatal, Catal. Layers Fundam. Appl. (2008) 89–129.
[47] J. Zaanen, G. Sawatzky, Band gaps and electronic structure of transition-metal compounds, Phys. Rev. Lett. 55 (1985) 418–421.
[48] F.M. Company, Electrical conductivity in sputter-deposited chromium oxide coatings, Thin Solid Films 127 (1985) 241–256.
[49] R.E. Meyer, Cathodic processes on passive zirconium, J. Electrochem. Soc. 107 (1960) 847, https://doi.org/10.1149/1.2427525.
[50] V. Viswanathan, K.S. Thygesen, J.S. Hummelshj, J.K. Nrskov, G. Girishkumar, B.D. McCloskey, A.C. Luntz, Electrical conductivity in Li 2O 2 and its role in determining capacity limitations in non-aqueous Li-O 2 batteries, J. Chem. Phys. 135 (2011).